Chemical Science

Accepted Manuscript

Chemical
Science

rsc.li/chemical-science

ISSN 2041-6539

ROYAL SOCIETY
OF CHEMISTRY

EDGE ARTICLE
Xinjing Tang et al.
Caged circular siRNAs for photomodulation of gene
expression in cells and mice

Volume 9
Number 1
7 January 2018
Pages 1-268

ROYAL SOCIETY
OF CHEMISTRY

rsc.li/chemical-science

Journal Name

ARTICLE

One-dimensional fluorescent covalent organic frameworks rich in exposed sp³-N sites for ultra-fast iodine capture and visual monitoring

Ke Li and Bing Yan*

Up to date, capturing radioactive iodine from nuclear waste remains an important issue in pollution control, especially for highly volatile CH_3I and I_2. With further research, covalent organic frameworks have shown great potential in iodine capture, and several COFs with high adsorption capacities have been reported. However, improving the capture rate of gaseous iodine remains a major challenge at present. To this end, researchers have improved iodine capture rates by introducing macropores, nitrogen sites, and heteroatoms. Emergingly, 1D COFs are used in the field of catalysis due to their abundant exposed sites. Inspired by this, it is feasible to increase the exposure of N sites to improve the iodine capture rate. Herein, we report a strategy based on 1D COFs (COF-1D6 and COF-1D7) with the introduction of exposed sites, which significantly enhances the adsorption rates of I_2 and CH_3I, while maintaining a high loading capacity. In particular, COF-1D6 with completely exposed sites exhibited the $K_{80\%}$ of 1.07 $g \cdot g^{-1} \cdot h^{-1}$, far higher than other reported COFs adsorbents. Meanwhile, the excellent fluorescence of COF-1D6 also enabled visual monitoring of the CH_3I adsorption process. This work provides new insights into rapid iodine capture from the perspective of exposure sites.

Introduction

As the energy crisis looms, the development of new energy sources has become an inevitable necessity.[1] Nuclear energy, wind energy, solar energy, and other clean energy sources have become the main contributors to low-carbon power generation.[2,3] Of these, nuclear energy has higher energy density and controllability, enabling it the best candidate to replace traditional power generation.[4] However, radioactive pollutants (^{90}Sr, ^{137}Cs, ^{99}Tc, ^{85}Kr, ^{133}Xe, etc.) release into the environment through accidents or improper nuclear waste processing, disposal or storage[5-7] Among them, ^{129}I and ^{131}I seriously threatening human health due to their high radioactivity, biocompatibility, and long half-life.[8-10] Meanwhile, iodine commonly exists in the highly volatile form of I_2 and CH_3I, which may easily enter the human body through respiration and are difficult to capture.[11] Thus, the management of radioactive iodine and the efficient treatment of gaseous iodine in radioactive waste are of paramount importance. Due to the cumbersome operation and high consumption costs of traditional solution-based washing method, the adsorbent method has attracted various attention for its high efficiency.[12] To address the challenge of iodine capture, diverse adsorbent materials has been designed by researchers, such as silver-based nanomaterials,[13-15]

modified biochar,[16] metal oxo clusters,[17] zeolites,[18] aerogels,[19] metal-organic frameworks (MOFs),[20,21] hydrogen-bonded organic frameworks (HOFs)[22,23] and covalent organic frameworks (COFs).[24-27] The adsorption of iodine mainly depends on metals that are compatible with iodine or the rich N sites. However, considering the cost of precious metals and the risk of potential secondary pollution from metal ions, the design of materials rich in N-sites and non-metallic with high adsorption performance has initiated a new era of iodine capture.[28]

COFs, as outstanding representatives of crystalline porous materials,[29,30] are widely used as adsorbents due to their stability, high specific surface area, and rich pore structure.[31,32] The pre-design and numerous synthetic units of COFs provide sufficient synthesis approach of diverse adsorbents for specific target, by means of flexible functional group combination, modification of different topologies and dimensions. Among the many types of COFs, imine-based COFs are synthesized through the Schiff base reaction and rich in imine N active sites for I_2 and CH_3I capture.[33] On this basis, different types of N sites can be further introduced through the flexible combination of synthetic units to enhance iodine capture capacity.[34] Maximum adsorption capacity and adsorption rate are important indicators for evaluating iodine capture capacity. Recently, researchers have mainly focused on enhancing adsorption capacity by increasing N content,[35] enlarging specific surface area and pore volume, as well as introducing electron-rich impurity elements (O, S).[36] As for adsorption rate, Lu's group improved the mass transfer rate of COF-300 for I_2 vapor by introducing macropores.[37] Luo et. al proved that the introduction of the S element can improve the efficiency of I_2 electron formation into I_3^- and I_5^-, thereby accelerating the adsorption process. [36]

Shanghai Key Lab of Chemical Assessment and Sustainability, School of Chemical Science and Engineering, Tongji University, Siping Road 1239, Shanghai 200092, China. E-mail: byan@tongji.edu.cn.

ARTICLE

Wang's research group also proposed that sp³-N has a faster N-methylation reaction rate.[38] Inspired by above, the adsorption capacity and adsorption rate of COFs for iodine are determined by the abundance of N sites, volume, and mass transfer efficiency. However, although common 2D COFs have abundant N sites and objective specific surface areas, their regular pore structures and strong stacking restrict I_2/CH_3I molecules to pass through the pores and come into contact with N sites. When the pore space is narrow or blocked by iodine molecules, the adsorption efficiency is greatly reduced. [39] Fortunately, 1D COFs formed by C_4 units and C_2V are widely used in catalysis,[40-42] adsorption,[43] and fluorescent sensing[44] due to their abundant exposed sites, unidirectional charge transfer, and higher dispersibility.[45] The typical band topological structure and ordered one-dimensional channels of 1D COFs significantly increase the exposure of edge sites, thereby improving the mass transfer efficiency between target molecules and N sites. Therefore, increasing the exposure of active nitrogen sites to improve iodine adsorption efficiency is feasible and has not been reported before. Furthermore, in the actual use of adsorbents, it is very meaningful to be able to easily observe the adsorption process. Compared to 2D COFs, 1D COFs are more likely to exhibit excellent fluorescence properties,[46] which makes it possible to monitor the degree of adsorption using fluorescence visualization.

Herein, inspired by the above theories and reports, this work aims to construct an efficient adsorption platform for I_2 and CH_3I

through the strategy of exposing active sites, achieving the following specific purposes: (i) Construction of fluorescent N-rich 1D COFs (ii) Comparison of adsorption rates for I_2/CH_3I with different degrees of synthetic nitrogen site exposure. (iii) Enhancing the adsorption rate of CH_3I by introduction of a large number of sp³-N sites. (iv) Constructing 1D COFs fluorescence platform for visual monitoring of adsorption processes.

Results and discussion

To start with, we selected C_4 and C_2v synthetic units for the preparation of 1D covalent organic frameworks based on previous reports and theoretical calculations. Common C_4 monomers mainly include 4,4',4'',4'''-(pyrene-1,3,6,8-tetrayl)tetraaniline, 4',5'-bis(4-aminophenyl)-[1,1':2',1''-terphenyl]-4,4''-diamine, tetrakis(4-aminophenyl)ethene, N,N,N',N'-Tetrakis(4-aminophenyl)-1,4-benzenediamine and their analogues. Notably, COFs adsorbents for I_2 and CH_3I depend on abundant nitrogen sites, and sp³-N has been reported to have higher quaternization ability with CH_3I, compared with sp²-N. To this end, we chose N,N,N',N'-Tetrakis(4-aminophenyl)-1,4-benzenediamine (TABA) rich in sp³-N. Subsequently, 4,4'-diformyltriphenylamine (DTPA) and 2,9-bis[p-(formyl)phenyl]-1,10-phenanthroline (BPPT) were selected to prepare COF-1D6 and COF-1D7 for following purposes.
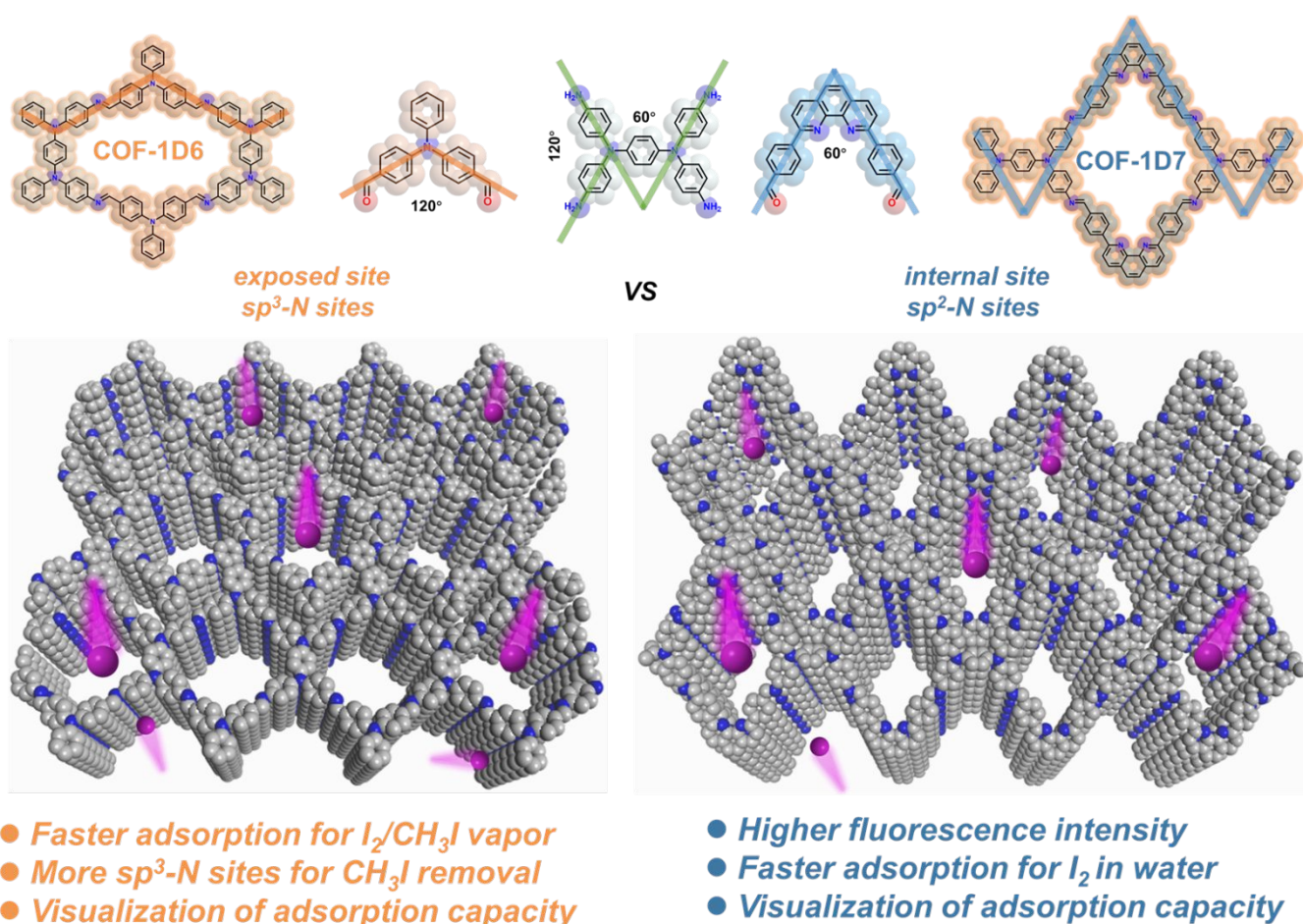
Scheme 1. Synthetic strategies and structural skeleton of COF-1D6 and COF-1D7, schematic diagram of I_2/CH_3I (purple balls) transport mode.

Phenanthroline group contains sp²-N site and higher conjugate flatness, endowing COF-1D7 with strong π-π stacking ability results in a more distinct pore structure. In contrast, 4,4'-diformyltriphenylamine containing sp³-N is not a regular plane, which may weaken the interlayer stacking of COF-1D6. Furthermore, as shown in Scheme 1, the N site in 4,4'-diformyltriphenylamine is exposed outside the COFs pores, which greatly increases the possibility of contact with I_2 and CH_3I, may enable COF-1D6 to achieve higher mass transfer efficiency when adsorbing gaseous I_2 and CH_3I. In summary, the designed COF-1D6 and COF-1D7 were expected to explore the effect of N-site exposure degree on the iodine adsorption process, as well as the adsorption ability of sp²-N and sp³-N active sites for iodine. Last but not least, DTPA and BPPT are excellent fluorescent units, which makes it possible to build luminescent 1D-COFs for visual fluorescence monitoring of adsorption processes.

When constructing 1D COFs, the sum of the interior angles formed by the C_4 unit and the V-shaped C_2 unit should be 180°.

DTPA and BPPT presenting different molecular angles (120° and 60°), which results that the two must be connected at 60° and 120° direction of TABA, respectively. Fortunately, these two different connection methods allow the relatively small-size A unit to form the hole wall with the long side of TABA, while small-size A unit form the pore wall with short side. The clever combination of the three makes 1D6 and 1D7 have similar pore sizes, eliminating the variable of pore size for subsequent comparative experiments.

As proof, powder X-ray diffraction (PXRD) was carried out to investigated the crystal structure of the COFs (Figures 1 a, d). COF-1D6 signal peak at 4.18 and 4.92° confirmed the existence of microporous structures, corresponding the (2 0 0) and (1 -1 0) crystal plane. The remaining minor peaks at 7.40, 8.26, 8.76, 11.32, 12.00, 16.17 and 21.17° belong to the (3 1 0), (4 0 0), (0 2 0), (5 -1 0), (4 2 0), (7 -2 0) and (4 1-1) crystal plane, respectively. Meanwhile, the characteristic peaks at 4.72, 5.32, 9.42, 12.65, 13.44, 15.80, 19.52 and 24.70 of COF-1D7 correspond to the (1 1 0), (2 0 0), (0 2 0), (4 2 0), (3 3 0), (2 2 -1), (4 2 0), (6 0 -1) crystal planes, respectively.

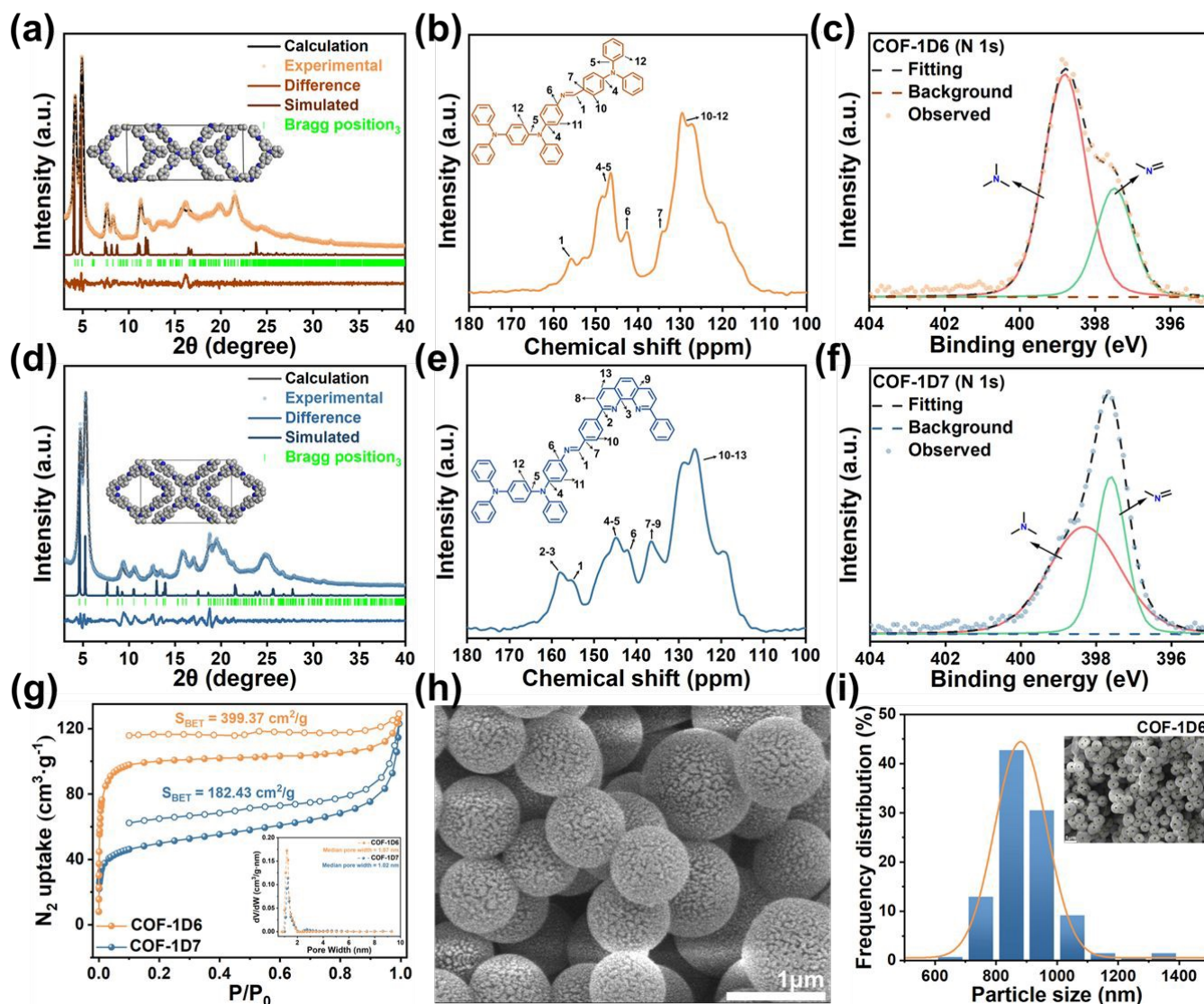**Figure 1**. Powder X-ray diffraction (PXRD) patterns for (a) COF-1D6 and (d) COF-1D7. Solid-State ¹³C CP-MAS of (b) COF-1D6, (e) COF-1D7. N 1s XPS spectra of (c) COF-1D6 and (f) COF-1D7. (g) N_2 adsorption–desorption curves and pore size distribution curves (inset) of COF-1D6 and COF-1D7. (h) SEM images of COF-1D6. (i) Diameter statistics of COF-1D6.

Chemical Science Accepted Manuscript

Then Materials Studio was conducted to perform the geometrical optimization of the structural models, and fit experimental PXRD patterns by Pawley refinement, obtaining the unit cell parameters for COF-1D6 (a = 43.79, b = 20.30, c = 3.84 Å; α = 93.61, β = 98.18, γ = 90.48°, with a Rwp of 4.82% and a Rp of 3.67%) and COF-1D7 (a = 36.52, b = 25.15, c = 4.81 Å; α = 90, β = 88.10, γ = 90°, with a Rwp of 6.25% and a Rp of 4.85%). Furthermore, to investigate the chemical stability of the two COFs, PXRD was performed for the COFs after immersion in different solutions for 48 h such as water N,N-Dimethylformamide (DMF), acetonitrile (ACN), dimethylsulfoxide (DMSO) 1M HCl and 1M NaOH. As shown in Figure S3, S4, apart from NaOH aqueous solution and DMSO having a slight effect on the crystallinity of both COFs, the materials remain stable in other solvents.

To explore the specific surface areas and pore sizes, N_2 adsorption–desorption experiments were performed at 77 K to characterize the porous structures of the two COFs. As shown in Figure 1g, the curves both indicated a typical isotherm of type IV, revealing the mesoporous characteristic of them. Furthermore, the pore size distributions of COF-1D6 and COF-1D7 displayed the pore sizes were mainly around 1 nm (Figure 1g inset, Figure S5), and the median pore widths of them were 1.07, and 1.02 nm, respectively proving that the two COFs have similar pore sizes. In addition, the single pore size distribution indicates that both COFs are one-dimensional in configuration and extend unidirectionally. Correspondingly, Brunauer–Emmett–Teller (BET) surface areas of them were calculated to be 399.27 (COF-1D6) and 182.43 (COF-1D7) m^2g^{-1}, with the pore volumes of 0.196 and 0.180 cm^3g^{-1}, respectively.

In order to further demonstrate the successful synthesis of COFs, Fourier transform infrared (FT-IR) spectroscopy was conducted on COF-1D6, COF-1D7 and their synthetic monomers (Figure S6, S7). In comparison to the ligands, the signal peaks around 3456-3349 cm^{-1} (-NH$_2$) of TABA, 1670 cm^{-1} (-CHO) of DTPA and 1691 cm^{-1} (-CHO) of BPPT almost completely disappeared in the FT-IR spectra of COF-1D6 and COF-1D7, explaining the thoroughness of the imine condensation reaction. In addition, Solid ^{13}C solid-state nuclear magnetic resonance (^{13}C NMR) also provides evidence for the formation of imine bonds. As shown in Figures 2b, e, the peaks at around 156 ppm (label 1) corresponded to C of the imine bond proved that imine bonds exist in two COFs. Furthermore, C in COF-1D6 and COF-1D7 are in similar chemical environments, such as C in the C-N bond (label 4-6) and benzene ring (label 7-13). Notably, the spectrum of COF-1D7 contains distinct peaks at 158 ppm compared with COF-1D6, which is attributed to the C connected to N in the Phenanthroline group in COF-1D7. Moreover, the X-ray photoelectron spectroscopy (XPS) revealed. also confirmed the presence of N elements in different environments (Figures 1c, f). For this purpose, the peak of N 1s was deconvoluted into to peaks of N in C=N (around 397.5 eV) and C-N (around 399.0 eV), corresponding to sp^3-N and sp^2-N in COF, respectively. Notably, the relative strengths of the two are reversed in COF-1D6 and COF-1D7, which is due to the fact that COF-1D6 contains more sp^3-N units (TABA), while COF-1D7 contains more sp^2-N units (BPPT).

Then, thermogravimetric analysis (TGA) was carried out to verify of the thermal stability of COFs. In Figure S8, no significant weight loss was observed at the temperature below 450 ℃, which proved that COFs have the potential for iodine capture in 80 ℃ iodine vapor. Finally, we used Scanning electron microscopy (SEM) to observe the morphology of the two COFs. In Figures 1h, S9, we can clearly see that COF-1D6 exhibits uniform spherical nanoparticles, while COF-1D7 does not form a regular morphology. Zeta potentials
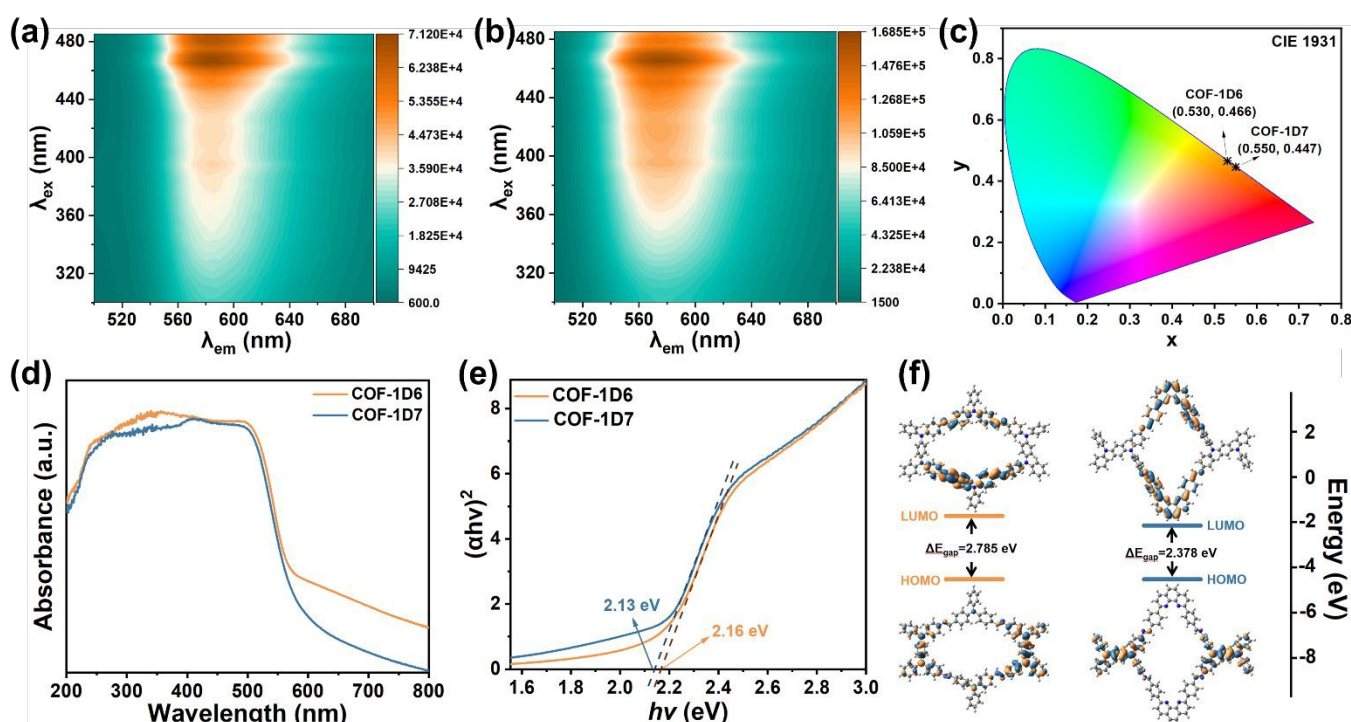

Figure 2. 3DEEM maps of (a) COF-1D6 and (b) COF-1D7. (c) CIE chromaticity coordinate, (d) UV–vis diffuse reflectance spectra, (e) Tauc plots and (f) HOMO and LUMO energy levels of COF-1D6 (orange) and COF-1D7 (blue).

also showed better particle stability for COF-1D6 (Figure S10). This may be due to the tetrahedral configuration of sp^3-N, which gives COF-1D6 better morphological plasticity, allowing it to stack into a more regular spherical shape during the solvothermal reaction. Based on diameter statistics of SEM image, the diameter of spherical COF-1D6 mainly ranges from 700 to 1000 nm (Figure 1i). This uniform spherical morphology also facilitates comparison of properties before and after adsorption of I_2 and CH_3I vapor. More specific elemental content and elemental distribution were also characterized by Energy-dispersive X-ray spectroscopy (EDS) and EDS mapping (Figures S11-S13), which shows that the material elements are evenly distributed and have a reasonable element ratio (C: 87.3 wt% N: 12.7 wt% for COF-1D6; C: 89.56 wt% N: 10.44 wt% for COF-1D7.).

In addition, considering potential fluorescent groups in both COFs and the relatively weak interlayer stacking of 1D COFs, the PL performance of them were further verified by emission-excitation spectra. As shown by 3DEEM maps in Figure 2a, b, the optimal excitation wavelengths for both are concentrated around 466 nm, while the optimal emission wavelengths are around 580 nm and 595 nm, respectively. Correspondingly, the CIE coordinates (Figure 2c) of COF-1D7 are in a redder position (0.550, 0.447) compared to COF-1D6 (0.530, 0.466). Since the two COFs lack the ability to form

intramolecular hydrogen bonds, the possibility of excited-state intramolecular proton transfer (ESIPT)[47] generating fluorescence is ruled out. Therefore, the fluorescence of the two COFs is mainly based on the intramolecular charge transfer (ICT) process, which requires the presence of a donor-acceptor pair and a fluorescent unit within the molecule. Consistent with the pre-design of the two COFs, the combination of TABA (D), DTPA (A), and BPPT (A) satisfies the requirements for the ICT process to occur. Notably, COF-1D7 exhibited higher fluorescence intensity. Solid UV-vis diffuse reflectance spectra were used to explain the underlying mechanism behind the above phenomenon. As shown in Figure 2d, the two COFs exhibit similar ultraviolet absorption spectra in the 200–800 nm range. Processing the spectrum by Tauc plot method (Figure 2e), we determined the values for the optical gap (Tauc gap) COF-1D6 (2.16 eV) and COF-1D7 (2.13 eV). The narrower optical bandgap indicated that COF-1D7 requires lower excitation energy, resulting in larger fluorescence emission wavelengths. In COF-1D7, BPPT is an electron-withdrawing group acting as an acceptor (A), while TABA is an electron-rich group acting as a donor (D). Under the excitation of ultraviolet light, electrons in COF-1D7 transfer more easily from D to A, compared to COF-1D6 which contains weak electron-withdrawing acceptor (DTPA). This greater degree of electron transfer makes it easier for electrons to pass through the
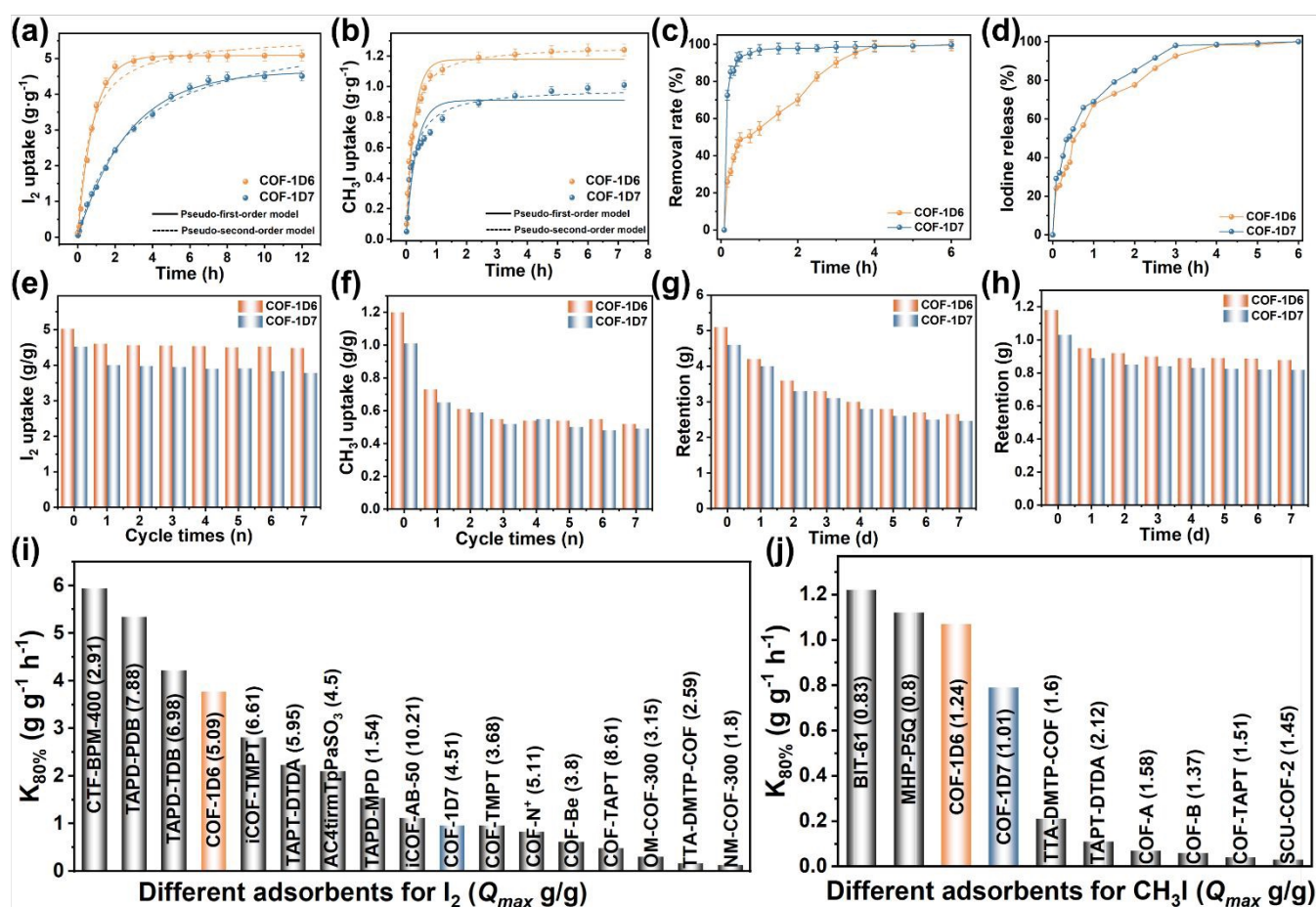

Figure 3. Equilibrium curve (a) iodine vapor, (b) methyl iodide vapor adsorption of COF-1D6 (orange) and COF-1D7 (blue) with adsorption kinetics curves fitting with pseudo-first-order model and pseudo-second-order model. (c) Kinetic study of iodine adsorption in water (C_0 = 100 ppm) and (d) iodine desorption in ethanol of COF-1D6 (orange) and COF-1D7 (blue). Regeneration cycles of COF-1D6 and COF-1D7 for (e) I_2 and (f) CH_3I. Retention curve at room temperature of COF-1D6 and COF-1D7 for (g) I_2 and (h) CH_3I. Comparison of $K_{80\%}$ values of several adsorbents for (i) I_2 and (j) CH_3I and their adsorption capacity in brackets. (corresponding references are presented in Table S3, S4.)

fluorescent group, thereby increasing the intensity of fluorescence emission. As verification, density functional theory (DFT) calculation was performed to calculate the HOMO–LUMO energy levels for structural units of COFs (Figure 2f). The relative magnitude of the ΔE_{gap} between the two (2.785 eV for COF-1D6, 2.378 eV for COF-1D7) is consistent with the Tauc gap. At the same time, in the excited state (LUMO), the electrons in COF-1D7 are more concentrated in the A unit, indicating that the electrons are transferred more completely. The combination of theory and practice clearly illustrates that stronger electron-withdrawing ability of A unit leads to narrower band gap, thereby facilitating the transfer of electrons to the A unit under excitation. When the fluorescent group is close to A or acts as the A unit itself (BPPT), the fluorescence emission intensity increases ($I_{1D7} > I_{1D6}$). Fitting of the time-resolved photoluminescence (TR-PL) spectra at room temperature provides fluorescence lifetimes of 5.67 and 5.46 ns (Figure S14), corresponding to the decay COF-1D6 and COF-1D7, respectively. The long fluorescence lifetime indicates that both COFs have excellent ability to provide excited electrons for reduction process during adsorption.

Based on the structural design of the COFs and successful preparation proven by above characterization, adsorption experiments were performed to explore the potential of COF-1D6 and COF-1D7 for I_2 and CH_3I capture. As shown in Figure S15, S16, two orange-red COFs turned black after being exposed to iodine vapor (75 °C) for a short time, demonstrating extremely strong iodine capture capabilities. COF-1D6 and COF-1D7 reached

adsorption saturation at around 2 hours and 7 hours (Figure 3a), with adsorption capacities of 5.09 and 4.51 g/g and the $k_{80\%}$ (evaluated at 80% of the full capacity) of 3.77 and 0.962 $g \cdot g^{-1} \cdot h^{-1}$, respectively. Fast adsorption rates and high adsorption capacities enable COF-1D6 comparable to common high-performance iodine adsorption materials (specific adsorption rates and adsorption capacities are shown in Figure 3i Table S3) Adsorption kinetics fitting shows that the adsorption equilibrium curves of the two COFs are more consistent with pseudo-first-order kinetic adsorption model ($R^2_{COF-1D6}$ = 0.998, $R^2_{COF-1D7}$ = 0.995), explained that iodine vapor is adsorbed by COFs in the form of physical enrichment. Since iodine also causes significant visual pollution in water, we also investigated the removal efficiency of the two materials for iodine in water (Figure 3c S17). Contrary to I_2 vapor capture, COF-1D7 showed a higher removal rate, which stems from better dispersibility of COF-1D7 in water compared to COF-1D6.

The large number of sp³-N sites introduced in our structural design enables efficient adsorption of CH_3I. Since methyl iodide is more volatile than iodine vapor, it is imperative to investigate the adsorption capacity of the two COFs for methyl iodide at room temperature. It is worth mentioning that both COFs showed extremely short equilibrium times, especially for COF-1D7, reaching adsorption saturation within two hours (Figure 3b). Unlike I_2 adsorption, the adsorption kinetics curve of CH_3I is more consistent with pseudo-second-order kinetic adsorption model ($R^2_{COF-1D6}$ = 0.994, $R^2_{COF-1D7}$ = 0.957), indicating that the adsorption of CH_3I is mainly a chemical process. The maximum adsorption of COF-1D6

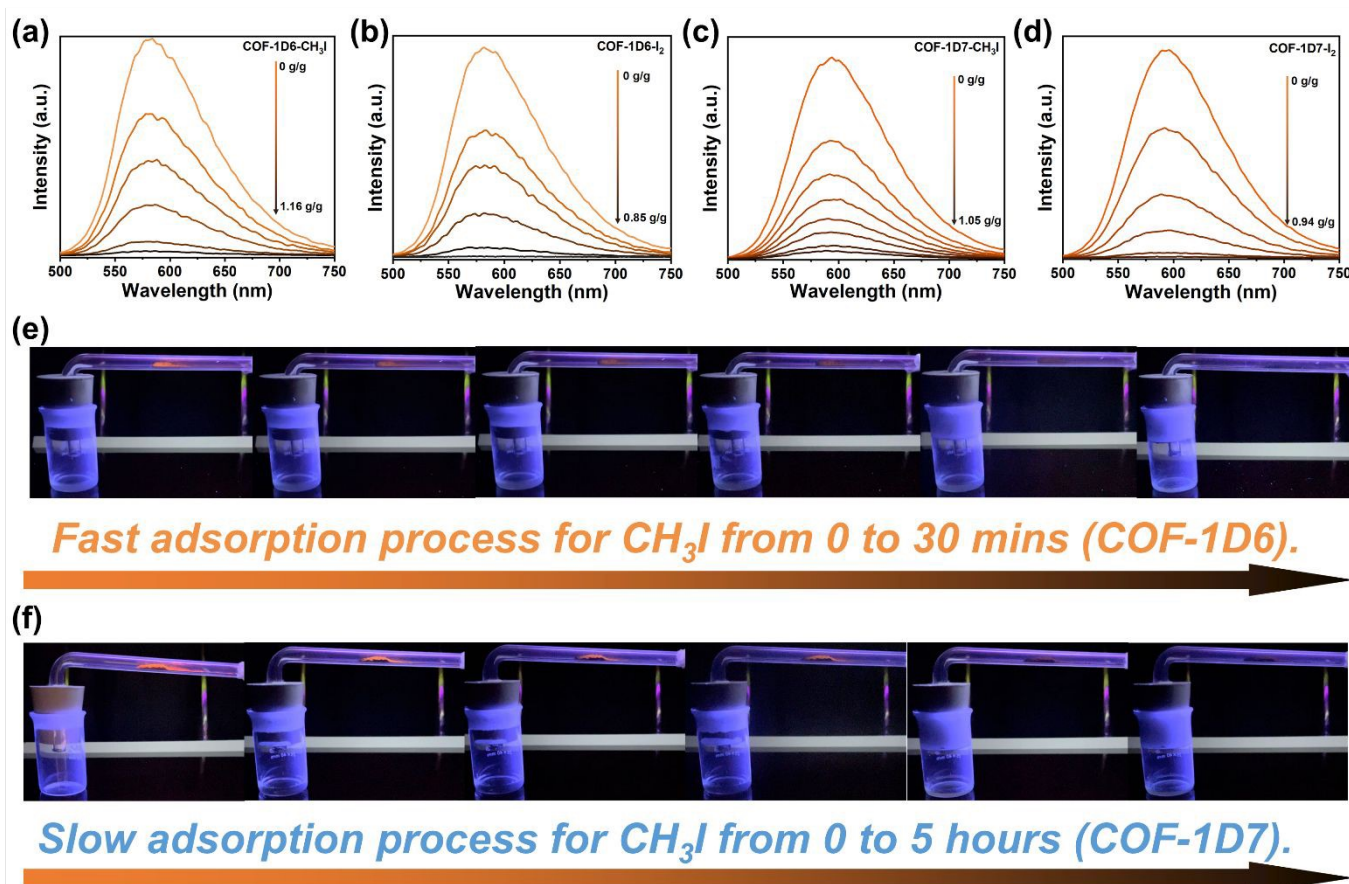**Figure 4.** Trend of fluorescence intensity with changes in adsorption capacity of COF-1D6 for (a) CH_3I and (b) I_2 and COF-1D7 for (c) CH_3I and (d) I_2. Visual monitoring of CH_3I adsorption process of (e) COF-1D6 and (f) COF-1D7.

and COF-1D7 reached 1.24 and 1.01 g/g, exhibiting ultra-high $K_{80\%}$ of 1.07 and 0.79 $g \cdot g^{-1} \cdot h^{-1}$. Such high adsorption rates and substantial adsorption capacities make COF-1D6 and COF-1D7 the fastest COFs materials for CH_3I adsorption, second only to Metal–Organic Framework adsorbent (BIT-61)[48] and multi-microporous organic polymers adsorbent (MHP-P5Q).[49] (Figure 3j, Table S4). The recyclability of adsorbents is an important indicator of their practical application capabilities. We first conducted iodine desorption experiments in ethanol and monitored the desorption process through UV-Vis spectroscopy (Figure S18). As shown in Figure 3d, both COFs loaded with iodine can reach desorption saturation within three hours. Based on their desorption performance in in ethanol, the two COFs materials were used in seven cycles of I_2 adsorption and desorption (washed by n-hexane). Both COFs maintained 85% of their maximum adsorption capacity in the seventh cycle (Figure 3e). However, the adsorption capacity of CH_3I retained only around 50% of its maximum after the second cycle (Figure 3f), which may be due to chemical interaction with part of N sites on COFs. After placing the two materials loaded with I_2 and CH_3I for seven days, approximately 40% of the I_2 escaped from both COFs (Figure 3g), while less than 20% of the CH_3I escaped (Figure 3h). It shows that both COFs have good retention capabilities for I_2 and CH_3I at room temperature.

Both materials exhibit excellent adsorption properties. COF-1D6 demonstrates higher adsorption capacity and faster adsorption rates for I_2 and CH_3I vapors, while COF-1D7 exhibits faster removal rates for I_2 in water, offering significant potential for practical applications in iodine capture. Once the adsorbent reaches

adsorption saturation in actual application, it must be replaced to achieve the goal of continuous treatment of pollutants. Therefore, it is essential to find a convenient and intuitive method to monitor the adsorption process. Fortunately, both adsorbents exhibited excellent fluorescence properties, which made it possible to determine the degree of adsorption based on fluorescence changes. As shown in Figures 4a-d, the fluorescence of COF-1D6 was completely quenched after adsorption of 116 wt % CH_3I and 85 wt % I_2. Similarly, the fluorescence of COF-1D7 also thoroughly disappears after adsorption of 105 wt % CH_3I and 94 wt % I_2. For I_2, when the fluorescence of the adsorbent is completely quenched, only about 20% of the maximum adsorption capacity is reached, so it is not possible to effectively monitor the entire adsorption process. Conversely, for the adsorption of CH_3I, fluorescence quenching corresponds precisely to the saturation adsorption amount. Therefore, it is entirely feasible to monitor CH_3I throughout the process using the fluorescence quenching of COF-1D6 and COF-1D7. To this end, we constructed a simple glass tube sealing device for direct capture of real-time fluorescent images under UV light (360 nm) (Figures 4e, f). The fluorescence emitted by COF-1D6 completely disappears within 30 minutes, as shown in Figure 4e, indicating that COF-1D6 reaches adsorption saturation in this device in just 30 minutes. As a control experiment (Figure 4f), COF-1D7 required 5 hours to be completely extinguished under the same conditions. The adsorption rate observed by fluorescence quenching and the adsorption equilibrium curve obtained by the weighing method show similar trends. The above clearly demonstrates that the fluorescence of COF-1D6 can be used for

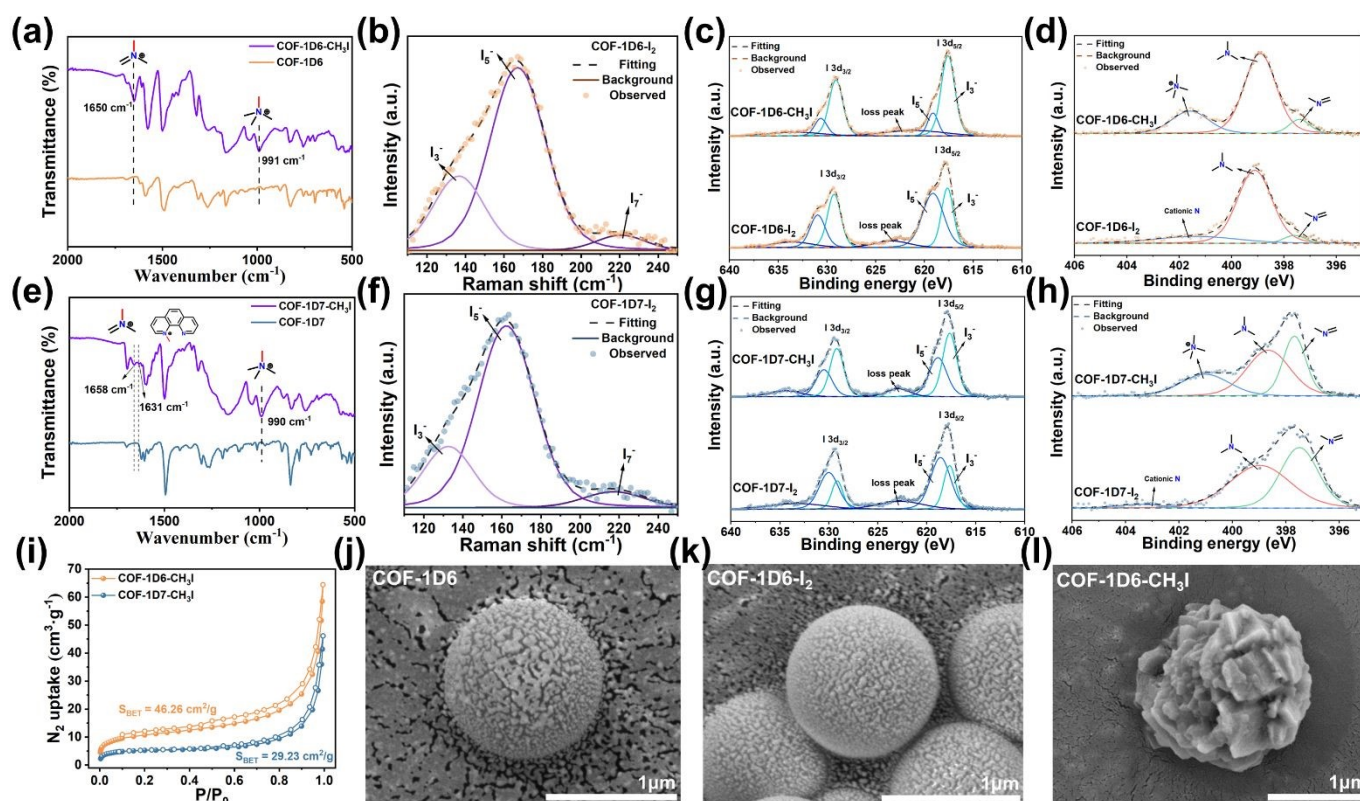**Figure 5.** FT-IR spectra of (a) COF-1D6 and (e) COF-1D7 before and after CH_3I adsorption. Raman spectra of (b) COF-1D6 and (f) COF-1D7. I 3d XPS and N 1S XPS spectra of (c, d) COF-1D6 and (g, h) COF-1D7 after I_2 and CH_3I adsorption. (i) N_2 adsorption–desorption curves of COF-1D6 and COF-1D7 after CH_3I adsorption. SEM images of (j) COF-1D6, (k) COF-1D6-I_2 and (l) COF-1D6-CH_3I.

efficient, visual monitoring of adsorption processes. In actual environments exposed to methyl iodide, simply shining a UV flashlight on COF-1D6 allows the adsorption process to be determined by the intensity of its fluorescence without coming into contact with the adsorbent.

Given that both materials exhibit excellent capture capabilities for I_2 and CH_3I as well as fluorescence quenching phenomena, instrumental characterizations such as XRD and XPS was used to investigate the possible adsorption mechanisms. The XRD patterns show that the characteristic peaks of both COFs disappear after adsorption of I_2 and CH_3I (Figure S19), and no characteristic peaks of elemental iodine appear, indicating that the adsorbed iodine filled in the channels and interlayers of the COFs in the form of amorphous ions. Compared to raw COFs, new peaks in the Raman spectra were deconvoluted into three peaks (around 125, 170 and 220 cm^{-1}), corresponding to I_3^-, I_5^- and I_7^- of COF-1D6-I_2 (Figure 5b) and COF-1D7-I_2 (Figure 5f), respectively. In the contrary, COFs did not exhibit new peaks in Raman spectra after CH_3I capture (Figure S20). FT-IR was used to analyze the functional groups after adsorption. After adsorption of iodine vapor, the infrared peak signals of both materials were largely obscured by iodine, and no new peaks were observed (Figure S21). However, compared with the original COFs (Figure 5a), COF-1D6-CH_3I exhibits signal peaks at 991 and 1650 cm^{-1} corresponding to the quaternization of sp^3-N sites and N sites in imine bonds, respectively. Meanwhile, FT-IR spectrum (Figure 5e) of COF-1D7-CH_3I shows additional peaks at 1631 cm^{-1} corresponding to the sp^2-N site in phenanthroline undergoing quaternization. Obviously, the peak intensity of sp^3-$N^+CH_3I^-$ is much higher than that of the other two characteristic peaks, indicating that the sp^3-N site is the main reaction site for CH_3I. Consistent with the FT-IR spectra, the XPS spectra (Figures 5d, h) of

both COFs after adsorption of CH_3I showed distinct characteristic peaks of quaternary ammonium N, while no significant N^+ appeared after I_2 adsorption. Therefore, based on the adsorption kinetics fitting results, the adsorption of CH_3I by COFs depends on the quaternization reaction, which corresponds to chemical adsorption. The capture of I_2 depends on its binding to N sites and the continuous formation of high-iodine complexes through halogen bonds, which is a physical adsorption process. This explanation also corresponds well with the existence state of I after COFs adsorb I_2 and CH_3I, which mainly exist in the form of high-iodine complexes (I_3^-, I_5^- and I_7^-) (Figures 5c, g) and low-iodine ions (I^-, I_3^-), respectively. The chemical reaction between COFs and CH_3I also explains the poor cycle capacity for CH_3I. Once saturation adsorption is reached for the first time, the N sites are occupied and cannot be physically desorbed. Therefore, during the second adsorption, there are no longer any quaternary ammonium reaction sites, resulting in a significant decrease in adsorption capacity. Compared with I_2 capture, the XRD characteristic peaks of the two COFs did not recover after desorption of CH_3I, indicating that the crystal structure had changed Figure S22. At the same time, the specific surface area of the material also decreased significantly after the first adsorption of CH_3I, and its morphology also significantly changes, especially for COF-1D6 which has a spherical structure (Figures 5j-l, S23). EDS and EDS mapping showed that both COFs have a uniformly high loading capacity for I_2/CH_3I (Figures S24-S29). Based on the above characterization, we further investigated the reasons for the fluorescence quenching of the two COFs and the more efficient adsorption capacity exhibited by COF-1D6 through DFT calculations. Firstly, fluorescence lifetimes of COF-1D6-I_2, COF-1D7-I_2, COF-1D6-$N^+CH_3I^-$ and COF-1D7-$N^+CH_3I^-$ were performed (Figures S30, S31). Compared with the original COFs, their
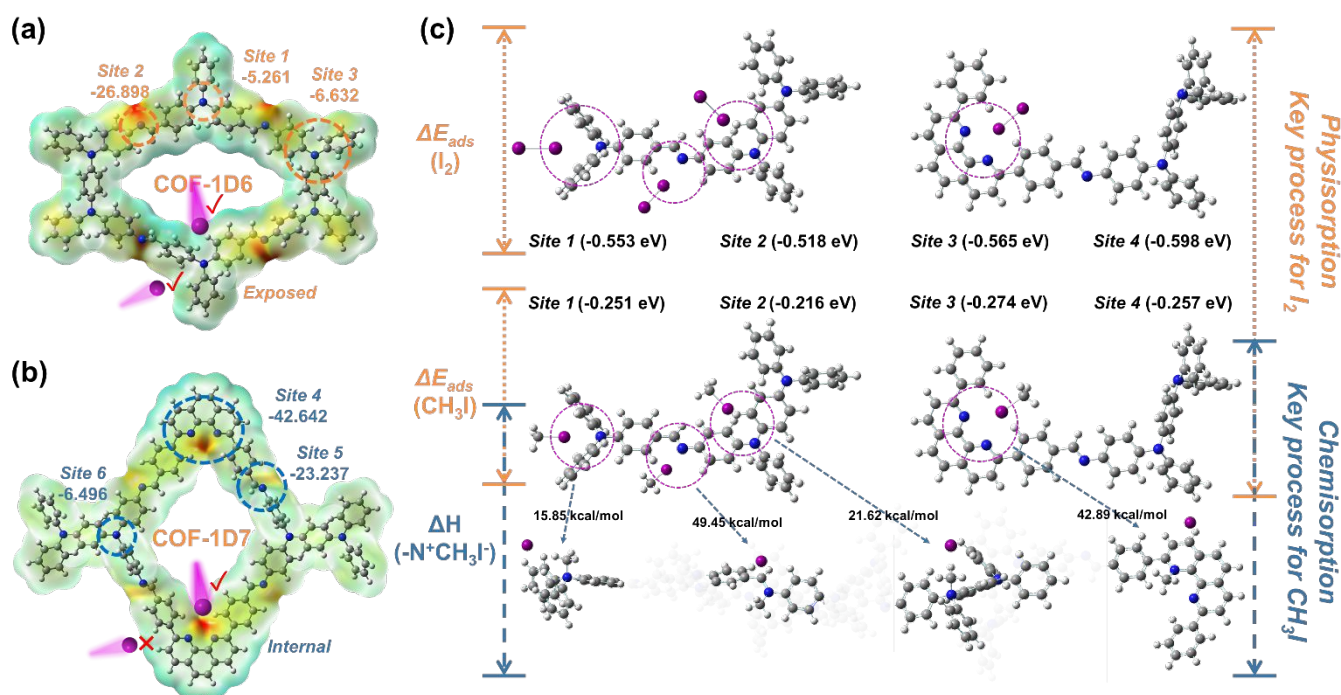
Figure 6. Electrostatic potential (ESP) and specific electrostatic potential energy and exposure and internal sites diagram of (a) COF-1D6 and (b) COF-1D7. (c) adsorption energies of I_2 and CH_3I at Sites 1–4 and enthalpy changes of quaternary ammonium reactions with CH_3I.

Journal Name

fluorescence lifetime did not weaken. At the same time, combining the LUMO-HOMO energy level comparison of the original COFs fragments and I_2 basically ruled out the photoinduced electron transfer (PET) process. Notably, the quenching ability of I_2 comes from the large amount of adsorption on the COFs surface during the adsorption process and the strong light absorption ability of dark-color iodine. Unlike this, CH_3I is a colorless vapor, so IFE and PET processes have been essentially ruled out. Therefore, we constructed quaternary ammonium sites at characteristic sites on the two COFs, performed LUMO-HOMO energy level (Figure S32, S33) of the molecular fragments before and after CH_3I adsorption. For COF-1D6, the ability to accept and donate electrons D and A units is similar. After the quaternization reaction occurs, the original A unit is converted into a relatively electron-rich unit, resulting in a D-A shift (Figure S34). Therefore, excited electrons no longer accumulate in the fluorescent unit, causing fluorescence quenching. In contrast, because BPPT exhibits strong electron-withdrawing properties, COF-1D7-$N^+CH_3I^-$ was generated and used as unit A. However, due to a decrease in electron acceptance, the excited state electrons were more concentrated in the N^+I^- region, resulting in fluorescence quenching. In summary, the effect of CH_3I affected the original ICT process, which may be the main quenching mechanism.

To further illustrate the higher adsorption rate exhibited by COF-1D6, Electrostatic potential (ESP) was used to reveal potential adsorption sites[50]. As shown in Figures 6a, b, Both COFs exhibit six active nitrogen sites, namely Sites 1–3 (-5.216, -26.898 and -6.632 eV) for COF-1D6 and Sites 4–6 (-42.642, -23.237 and -6.496 eV) for COF-1D7. Given the similarities between Sites 2, 3, 5, and 6, we mainly compared the differences between Site 1 and Site 4. As originally designed in Figure 6a, Site 1 serves as the exposed site, and the vapor molecules of I_2 and CH_3I can interact with Site 1 through adsorption by either transporting in the channels of COF-1D6 or by free thermal motion in the gaps between the 1D COF bands. In contrast, N on Site 4 can only come into contact with molecules transported through the channel. The introduction of these exposed sites greatly accelerated the adsorption rate of steam molecules. In fact, the other four sites existing simultaneously in both COFs, also possess the characteristics of exposed sites due to the unidirectional extension properties of 1D COFs. This is why both types of COFs exhibit high adsorption rates, with COF-1D6 performing even better. Inspired by previous reports,[37] we also verified the advantages of exposure sites from the perspective of adsorption capacity. We assume that when adsorption is saturated, the micropores of COFs are completely filled with I_2. Thus, the theoretical adsorption capacity was calculated from the micropore volumes of COF-1D6 (0.196 cm^3/g) and COF-1D7 (0.180 cm^3/g) with the solid iodine density (4.93 $g·cm^{-3}$). The results were 0.966 and 0.887 g/g, respectively, far below the actual saturation adsorption capacity of COF-1D6 (5.09 g/g) and COF-1D7 (4.51 g/g). The above results strongly prove that the adsorption of iodine by the two COFs does not only occur in the micropores, but more often at exposed sites which are conducive to further enrichment of iodine in the gaps between 1D COFs bands. In addition to their spatial structural advantages, all four sites have been proven to have excellent adsorption capabilities for I2 and CH_3I. Based on DFT calculations (Figures S35-S46), the adsorption

energies (E_{ads}) of iodine at Sites 1–4 are -0.553, -0.518, -0.565 and -0.598 eV, respectively. Meanwhile, the adsorption energies (E_{ads}) of Sites 1–4 with CH_3I were calculated as -0.251, -0.216, -0.274 and -0.257 eV, respectively. Considering that CH3I adsorption is based on quaternary ammonium reactions, we additionally calculated the enthalpy changes (ΔH) of quaternary ammonium reactions at Sites 1–4, which are 15.85, 49.45, 21.62 and 42.89 kcal/mol. As Site 1 and Site 3 of sp^3-N, the energy barrier of the reaction is much lower than that of sp^2-N. This result responds to the expected design, consisting with previous reports and infrared spectroscopy results. Therefore, the characteristics of the 1D COF exposure sites and the ultra-high sp^3-N content guarantee COF-1D6 the most efficient COF-type adsorbent for CH_3I.

Conclusions

In summary, we constructed two fluorescent N-rich 1D COFs through selection of synthesis unit, which contain exposed sp^3-N sites (COF-1D6) and non-exposed sp^2-N sites (COF-1D7), respectively. The two COFs exhibit excellent capture ability for I_2/CH_3I due to their abundant N sites and the band topology characteristic of 1D COFs. Compared to COF-1D7 (4.51 for I_2, 1.01 for CH_3I), COF-1D6 exhibits higher adsorption capacities for both I_2 (5.09) and CH_3I (1.24 g/g). Using $K_{80\%}$ to represent the adsorption rate, COF-1D6 showed extremely high adsorption rates for I_2 (3.77 $g·g^{-1}·h^{-1}$) and CH_3I (1.07 $g·g^{-1}·h^{-1}$). Particularly, the adsorption rate of COF-1D6 for CH_3I is higher than all reported COF adsorbents. This outstanding property is attributed to the completely exposed sp^3-N sites in COF-1D6, which break through the limitation of molecular transport within the pore on adsorption efficiency. Meanwhile, the affinity and reactivity of the designed sp^3-N with CH_3I are also indispensable. In addition, the excellent fluorescence properties of the two COFs judiciously applied to for visual monitoring of the CH_3I adsorption process. Based on 1D COFs, this work provides a new paradigm for improving adsorption rates by increasing the abundance of exposed sites.

Author contributions

B. Y. revised the manuscript. K. L. designed the experiment, prepared the materials, measured the adsorption properties, collected pictures, wrote the manuscript and completed the data simulation.

Acknowledgements

Notes and references

1   B. C. Gibb, *Nat. Chem.* 2025, **17**, 629-631.
2   S. Chu, A. Majumdar, *Nature* 2012, **488**, 294-303.
3   E. Kintisch, *Science* 2005, **310**, 1406-1406.
4   M. S. Dresselhaus, I. L. Thomas, *Nature* 2001, **414**, 332-337.

5   L. Feng, H. Wang, T. Liu, T. Feng, M. Cao, J. Zhang, T. Liu, Z. Guo, C. Galiotis, Y. Yuan, *Nat. Sustain.* 2023, **6**, 789-796.

6   D. Mei, L. Liu, B. Yan, *Coord. Chem. Rev.* 2023, **475**, 214917.

7   C. Xiao, Z.Hassanzadeh Fard, D. Sarma, T.-B. Song, C. Xu, M. G. Kanatzidis, *J. Am. Chem. Soc.* 2017, **139**, 16494-16497.

8   D. Banerjee, A. J. Cairns, J. Liu, R. K. Motkuri, S. K. Nune, C. A. Fernandez, R. Krishna, D. M. Strachan, P. K. Thallapally, *Acc. Chem. Res.* 2015, **48**, 211-219.

9   C. Muhire, A. Tesfay Reda, D. Zhang, X. Xu, C. Cui, *Chem. Eng. J.* 2022, **431**, 133816.

10   A. Saiz-Lopez, J. M. C. Plane, A. R. Baker, L. J. Carpenter, R. von Glasow, J. C. Gómez Martín, G. McFiggans, R. W. Saunders, *Chem. Rev.* 2012, **112**, 1773-1804.

11   Y. Lin, C. Wang, J. Wu, J. Tang, G. Ye, X. Zhao, H. Li, Y. He, *Small* 2024, **20**, 2401167.

12   G. Matthys, A. Laemont, N. De Geyter, R. Morent, R. Lavendomme, P. Van Der Voort, *Small* 2024, **20**, 2404994.

13   K. W. Chapman, P. J. Chupas, T. M. Nenoff, *J. Am. Chem. Soc.* 2010, **132**, 8897-8899.

14   H. W. Kang, J.-H. Choi, K. R. Lee, H.-S. Park, *J. Nucl. Mater.* 2021, **543**, 152635.

15   T. C. T. Pham, S. Docao, I. C. Hwang, M. K. Song, D. Y. Choi, D. Moon, P. Oleynikov, K. B. Yoon, *Energy Environ. Sci.* 2016, **9**, 1050-1062.

16   X. Wang, A. Li, J. Chang, F. Liao, H. Gao, J. Zhang, H. Fu, Y. Yang, Y. Liao, *Langmuir* 2024, **40**, 15107-15116.

17   G.-X. Yan, E.-X. Chen, J.-X. Yang, J. Zhang, Q. Lin, *Inorg. Chem.* 2025, **64**, 6935-6942.

18   Y. Lei, G. Zhang, Q. Zhang, L. Yu, H. Li, H. Yu, Y. He, *Nat. Commun.* 2021, **12**, 4483.

19   B. J. Riley, S. Chong, M. J. Olszta, J. A. Peterson, *ACS Appl. Mater. Interfaces* 2020, **12**, 19682-19692.

20   W. Xie, D. Cui, S.-R. Zhang, Y.-H. Xu, D.-L Jiang, *Mater. Horiz.* 2019, **6**, 1571-1595.

21   S. Chen, Y. Wang, J. Huang, H. Xie, J. Yuan, M. Song, B. Yang, Q. Pang, B. Tu, *ACS Mater. Lett.* 2025, **7**, 304-311.

22   Y. Lin, X. Jiang, S. T. Kim, S. B. Alahakoon, X. Hou, Z. Zhang, C. M. Thompson, R. A. Smaldone, C. Ke, *J. Am. Chem. Soc.* 2017, **139**, 7172-7175.

23   B. Li, W. Qiu, G. P. A. Yap, Y. L. Dory, J. P. Claverie, *Adv. Funct. Mater.* 2024, **34**, 2311964.

24   Y. Xie, T. Pan, Q. Lei, C. Chen, X. Dong, Y. Yuan, W. A. Maksoud, L. Zhao, L. Cavallo, I. Pinnau, *Nat. Commun.* 2022, **13**, 2878.

25   J. Chang, H. Li, J. Zhao, X. Guan, C. Li, G. Yu, V. Valtchev, Y. Yan, S. Qiu, Q. Fang, *Chem. Sci.* 2021, **12**, 8452-8457.

26   Y. Xie, T. Pan, Q. Lei, C. Chen, X. Dong, Y. Yuan, J. Shen, Y. Cai, C. Zhou, I. Pinnau, *Angew. Chem. Int. Ed.* 2021, **60**, 22432-22440.

27   M. Hao, Y. Xie, M. Lei, X. Liu, Z. Chen, H. Yang, G. I. N. Waterhouse, S. Ma, X. Wang, *J. Am. Chem. Soc.* 2024, **146**, 1904-1913.

28   N. Arora, T. Debnath, M. C. Senarathna, R. M. Johnson, I. G. Roske, G. A. Cisneros, R. A. Smaldone, *Chem. Sci.* 2024, **15**, 3571-3577.

29   W. K. Haug, E. M. Moscarello, E. R. Wolfson, P. L. McGrier, *Chem. Soc. Rev.* 2020, **49**, 839-864.

30   C. S. Diercks, O. M. Yaghi, *Science* 2017, **355**, eaal1585.

31   K. Li, D. Mei, Y.-s. Liu, B. Yan, *Chem. Mater.* 2025, **37**, 2535-2545.

32   X. Shen, B. Yan, *Adv. Funct. Mater.* **n/a**, 2424688. DOI: https://doi.org/10.1002/adfm.202424688.

33   P. Wang, Q. Xu, Z. Li, W. Jiang, Q. Jiang, D. Jiang, *Adv. Mater.* 2018, **30**, 1801991.

34   Y. Xie, Q. Rong, F. Mao, S. Wang, Y. Wu, X. Liu, M. Hao, Z. Chen, H. Yang, G. I. N. Waterhouse, *Nat. Commun.* 2024, **15**, 2671.

35   Y. Ma, J. Pan, H. Rong, L. Liu, Y. Zhang, X. Cao, J. Zhang, T. Liu, N. Wang, Y. Yuan, *Adv. Sci.* **n/a**, e00697. DOI: https://doi.org/10.1002/advs.202500697.

36   Y. Luo, Y. Qin, C. Ni, C. Liu, H. Yan, Y. Tao, W. Du, J. Zou, *Chem. Eng. J.* 2024, **497**, 154941.

37   T. Liu, Y. Zhao, M. Song, X. Pang, X. Shi, J. Jia, L. Chi, G. Lu, *J. Am. Chem. Soc.* 2023, **145**, 2544-2552.

38   L. He, B. Li, Z. Ma, F. Zhao, M. Zhang, J. Chen, L. Li, F. Tang, L. He, D. Wu, Y. Li, L. Chen, L. Chen, C. Zhao, K. Cao, X, Dai, Z. Chai, S. Wang, *ACS Cent. Sci.* 2024, **10**, 2072-2081.

39   K. Li, B. Yan, *Inorg. Chem.* 2025, **64**, 12722-12730.

40   J. Zhang, F. Xue, Z. Wang, *Angew. Chem. Int. Ed.* 2025, **64**, e202425617.

41   S. Yang, Z. He, X. Li, B. Mei, Y. Huang, Q. Xu, Z. Jiang, *Angew. Chem. Int. Ed.* 2025, **64**, e202418347.

42   C. Yang, J. Le, Y. Kuang, Z. Meng, H. Dai, Y. Zhou, H. Qiu, *J. Am. Chem. Soc.* 2024, **146**, 26198-26206.

43   Y.-Z. Cheng, X. Bao, D. Jiang, W. Ji, D.-H. Yang, X. Ding, X. Liu, Y. He, B.-H. Han, *Angew. Chem. Int. Ed.* 2025, **64**, e202414943.

44   X. Shen, B. Yan, *J. Mater. Chem. A* 2024, **12**, 6455-6464.

45   P. Huang, L.-H. Hou, M.-Y. Yang, C. Xiao, Y.-L. Wu, S-J. Cai, W.-J. Guo, M. Zhang, Lu, M.; Y.-Q. Lan, *Angew. Chem. Int. Ed.* 2025, **n/a**, e202507002. DOI: https://doi.org/10.1002/anie.202507002.

46   Z. Chen, K. Wang, Y. Tang, L. Li, X. Hu, M. Han, Z. Guo, H. Zhan, B. Chen, *Angew. Chem. Int. Ed.* 2023, **62**, e202213268.

47   Y. Wang, X.-Q. Ran, C. Yang, H.-L. Qian, X.-P Yan, *Anal. Chem.* 2024, **96**, 5608-5614.

48   D. Xu, Y. Ye, B. o. Li, R. Luo, J. Zhou, X. Ma, B. Wang, *Chem. Mater.* 2025, **37**, 238-246.

49   K. Jie, Y. Zhou, Q. Sun, B. Li, R. Zhao, D.-e. Jiang, W. Guo, H. Chen, Z. Yang, F. Huang, S. Dai, *Nat. Commun.* 2020, **11**, 1086.

50   X.-Q. Ran, C. Zhu, Q.-Y. Mao, S.-T. Xu, S.-P. Liu, P. Gu, Y. Jiang, X.-P. Yan, H.-L. Qian, *J. Mater. Chem. A* 2025, **13**, 13825-13831.

Data availability statements

- Additional data are made available in the supplementary information file.

- The datasets generated or analyzed during the current study are not publicly available due to the nature of the research but are available from the corresponding author on reasonable request.